ACS Photonics

Article

Cite This: ACS Photonics 2019, 6, 545−552

pubs.acs.org/journal/apchd5

Lithium Niobate Nanocubes as Linear and Nonlinear Ultraviolet Mie Resonators

Flavia Timpu,*[,†] Joan Sendra,[†,⊥] Claude Renaut,[†] Lukas Lang,[†] Maria Timofeeva,[†] Maria Teresa Buscaglia,[‡] Vincenzo Buscaglia,[‡] and Rachel Grange[†]

[†]Optical Nanomaterial Group, Institute for Quantum Electronics, Department of Physics, ETH Zürich, Auguste-Piccard- Hof 1, 8093 Zürich, Switzerland

[‡]Institute of Condensed Matter Chemistry and Technologies for Energy, National Research Council, Via De Marini 6, I-16149 Genoa, Italy

Supporting Information

ABSTRACT: Many dielectric and semiconductor materials used for all-dielectric resonators or metasurfaces have low absorption in the near-infrared to visible range, but they are lossy in the near-ultraviolet (NUV) range due to their low energy band gap. Contrary to this, the ferroelectric lithium niobate ($LiNbO_3$, LNO) has an energy band gap larger than 4 eV and, consequently, very low losses in the NUV range down to 310 nm. Here, we propose LNO nanocubes as a new alternative material for nonlinear photonics in the NUV range. We report that LNO nanocubes fabricated by solvothermal synthesis with sizes from 200 to 300 nm demonstrate strong second harmonic generation (SHG) emission below 400 nm due to Mie resonances, with an SHG enhancement of 10^7 compared to bulk LNO at 360 nm. The LNO nanocubes presented in this work are novel efficient all-dielectric Mie resonant nanostructures for the NUV with a wide range of possible photonic applications, from nanophotolithography to metasurfaces and complex assemblies of nanostructures or nano-optical modulators.

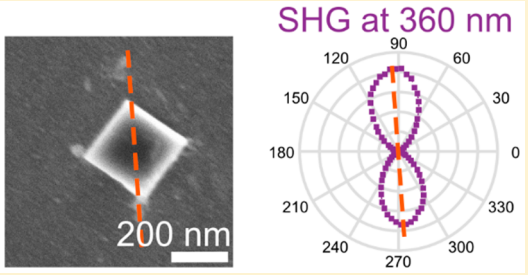

KEYWORDS: *nanophotonics, second-harmonic generation, Mie scattering, enhancement*

The development of photonics was marked by the invention of the laser and the subsequent demonstration of nonlinear optical phenomena, such as sum- and difference-frequency generation, third-harmonic generation, or optical parametric generation. These nonlinear phenomena are utilized in many applications from optical communication and optical parametric amplification to the development of multiphoton microscopy.[1]

In bulk materials, the wave propagation is linked to the wavelength-dependent refractive index. Hence, the nonlinear emission efficiency is high when phase-matching conditions are fulfilled.[2] Several solutions are proposed to achieve phase matching in a material, such as periodic poling,[3] quasi-phase matching,[2] or random phase matching.[4] Conversely, the phase mismatch can also be reduced if the refractive index of the material is close to zero. This exotic behavior is obtained in zero-index metamaterials, which are fabricated by structuring metal−dielectric composites at the subwavelength level.[5] Indeed, nanostructuring of bulk materials opened the way to photonic devices with new properties. In addition to metamaterials with exotic dielectric functions, nanostructuring is used to miniaturize optical components such as lenses, filters, or polarizers with tunable, switchable, or sensing functionalities.[6] The nanostructures forming these metamaterials have sizes smaller than the coherence length. Consequently, phase-matching techniques are not necessary and have no effect on their nonlinear emission efficiency. Furthermore, nanostructures can locally confine electromagnetic fields due to their small size. This confinement corresponds to resonances that occur at specific wavelengths that can be tuned by changing the size, shape, and material. Therefore, nanostructures have complex linear extinction spectra containing several electric and magnetic multipole resonances[7] that have been used to enhance light−matter interaction and nonlinear signal emission efficiency,[8−12] as well as to suppress the linear scattering cross-section in anapole-like modes.[13,14]

Metallic nanostructures with asymmetrical geometrical shapes have been successfully used as nonlinear emitters.[15] While such plasmonic nanostructures are rather easy to fabricate, their use is limited in the visible (VIS) range due to high ohmic losses.[16] Furthermore, noble metals have a centrosymmetric crystal structure and their second-order nonlinear optical properties originate only from the broken symmetry at the surface[17] or from higher-order multipole resonance effects.[18] Nanostructures fabricated from high refractive index dielectric materials such as silicon (Si), gallium arsenide (GaAs), or germanium (Ge) have been proposed as

Received: November 16, 2018
Published: January 11, 2019

DOI: 10.1021/acsphotonics.8b01594
ACS Photonics 2019, 6, 545−552

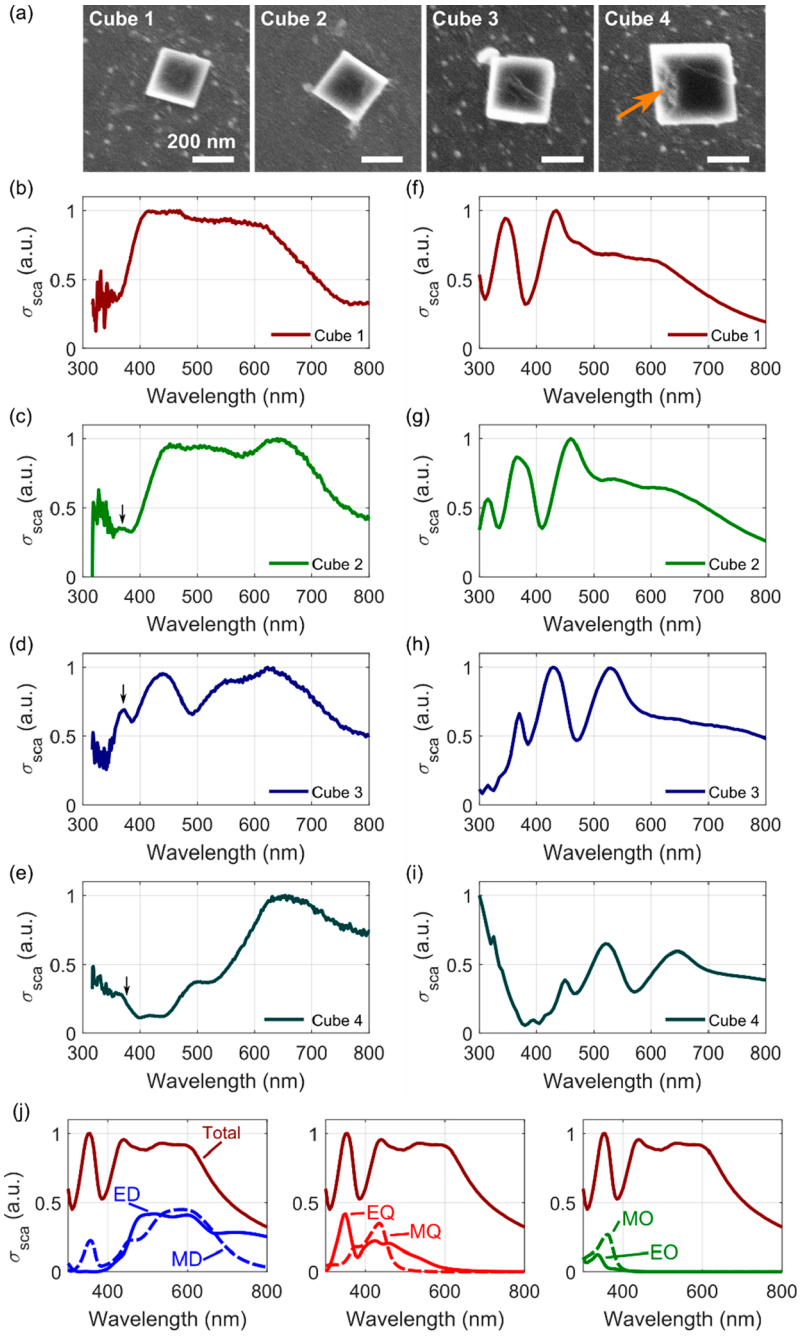

Figure 1. Scattering cross-section of single LNO nanocubes. (a) SEM micrographs of the isolated single nanocubes (cubes 1, 2, 3, and 4, respectively). The orange arrow indicates a defect along the edge of cube 4. (b–e) Measured scattering cross-section and (f–i) simulated scattering cross-section of the single LNO nanocubes from (a). The labels indicate the corresponding nanocubes. (j) Spherical multipole expansion calculated with the FEM model from the total scattering cross-section (solid red line) for the LNO nanocube 1. ED, electric dipole; MD, magnetic dipole; EQ, electric quadrupole; MQ, magnetic quadrupole; EO, electric octupole; MO, magnetic octupole.

an alternative without the ohmic losses of metals.[19−21] However, while some of these materials like GaAs possess bulk second-order nonlinearities, none of these materials have low losses in the VIS range. Furthermore, their performance decreases even more in the near ultraviolent (NUV) range due to absorption coefficients higher than 1 at 350 nm.[22] In conclusion, new second-order nonlinear materials for applications in the NUV−VIS range are required.

In this work, we propose using ferroelectric metal oxide lithium niobate ($LiNbO_3$, LNO) nanostructures as a new material for nonlinear photonic applications in the NUV−VIS range. In its bulk form, LNO is a transparent insulating material with a high energy band gap of 4 eV[23] and an absorption coefficient smaller than 10^{-5} at 350 nm.[24] Additionally, LNO has a hexagonal noncentrosymmetric crystal structure[25] with significant nonlinear effects such as piezoelectricity, electro-optical effect, and second-harmonic generation (SHG). Due to these nonlinear properties, LNO is an established material for microstructures and waveguides for nonlinear photonics applications such as optical modulators for telecommunications[26] or integrated tunable Bragg gratings.[27,28]

DOI: 10.1021/acsphotonics.8b01594
ACS Photonics 2019, 6, 545−552

Up to now, few studies have been performed on LNO nanostructures. Efforts have been directed toward fabricating nanometer-sized LNO nanostructures, mainly by bottom-up chemical synthesis.[29−36] The crystal structure of these LNO nanostructures is preserved down to diameters as small as 5 nm.[33] Cube-shaped LNO nanoparticles were demonstrated as viable probes for multiphoton imaging of biological samples.[36] Such nanoparticles with nonlinear optical properties, sometimes called harmonic nanoparticles, have been used as coherent subwavelength light emitters or nonresonant microscopy markers.[37,38] Their main advantages compared to fluorescent probes are the lack of bleaching and blinking, the emission of coherent photons, the reduced nonradiative losses, and the improved natural spectral separation of the emitted signal from the incident light. Also, since SHG is strongly linked to the crystal structure of the material, orientation-dependent polarization patterns can be measured.[39−41] Additionally, metal oxide nanoparticles are robust and chemically inert in many environments, which makes them biocompatible and nontoxic.[42,43] Harmonic nanoparticles employed in bioimaging have contributed to overcoming the limitations of various microscopy techniques, leading to improved resolution and detection sensitivity even in deep tissues or turbid media.[44,45] In the UV range, the biological samples have increased absorption cross-sections. This limits the usage of harmonic nanoparticles as markers for bioimaging, but opens possibilities for applications where high absorption is desirable, as in the case of theranostics and cancer cell apoptosis.[46] Harmonic nanoparticles are also successfully used to characterize, calibrate, and standardize the metrology of multiphoton microscopes with subdiffraction limit over a broad spectral range.[47]

Given the properties of harmonic nanoparticles listed above, the low absorption of LNO in the NUV, and the high quality of the crystal structure of LNO nanocubes compared to nanospheres,[35] we investigate LNO nanocubes for their potential for further applications in photonics beyond bioimaging as, for instance, new types of metasurfaces,[48,49] complex materials, nonlinear light converters,[50] integrated photonics,[51] or nano-optical modulators. Here, we show LNO nanocubes as Mie resonators and as efficient SHG emitters and demonstrate them as novel all-dielectric building blocks for nonlinear nanophotonics in the NUV range. We exploit the larger energy band gap of LNO that makes it transparent down to 310 nm.[23] Furthermore, LNO has an SHG coherence length of 2174 nm at a wavelength of 400 nm and an intrinsically non-centrosymmetric hexagonal crystal structure with a dominant component in the reduced second-order susceptibility tensor $d_{33} = -34$ pm/V.[23] We perform a full spectral characterization of LNO nanocubes with sizes between 200 and 300 nm fabricated by solvothermal synthesis and demonstrate their high SHG efficiency values between 1.7×10^{-7} and 7.6×10^{-7} 1/W at 360 nm in the NUV region. Additionally, we show that the SHG from single LNO nanocubes is enhanced 10^7 times compared to bulk LNO. We further show by SHG polarimetry that, compared to nanospheres, LNO nanocubes have predictable SHG emission patterns and crystal orientations when they are deposited with a face parallel to a flat substrate, which allows a better control of the building blocks for future applications.

RESULTS AND DISCUSSION

Fabrication of LNO Nanocubes. We fabricate LNO powders by a solvothermal synthesis method. We obtain powders containing LNO rhombohedra with sizes ranging from 100 to 400 nm. Examples of single LNO rhombohedra are shown in the SEM micrographs in Figure 1a. According to X-ray diffraction (XRD) measurements (Figure S1a), the crystal structure of the LNO rhombohedra corresponds to the hexagonal $R3c$ symmetry. High-resolution TEM images (Figure S1b) reveal that lattice planes with a separation of about 0.38 nm are parallel to the lateral faces of the rhombohedra. This interplanar distance is in good agreement with the value of 0.375 nm expected for the d-spacing of the (012) lattice planes calculated using the reference lattice parameters of LNO, $a = 0.5148$ nm and $c = 1.3863$ nm.[25] Because of the 3-fold symmetry of the hexagonal system, the faces of the rhombohedra correspond to three equivalent families of lattice planes, (012), (−102), and (1−12) having the same d-spacing (Figure S1c). These planes form an angle of 32.76° with the c-axis, i.e., the direction of the spontaneous polarization vector.[25] Therefore, the polarization axis of the LNO crystal is oriented along the diagonal of the rhombohedron in such a way that its projection on the lateral faces lies along their major diagonal. From the scanning electron microscopy (SEM) micrographs, we determine that the angles between the facets of rhombohedra have values of 93.8° and 86.7°, in good agreement with the angles formed by the planes (012), (1−12), and (−102) (Figure S1d). For simplicity, and since their width, length, and height are almost equal, the LNO rhombohedra are called LNO nanocubes in this work.

The samples for the optical measurements are prepared as follows. We spin coat a diluted suspension of LNO nanocube powder in ethanol on an indium tin oxide (ITO)-covered fused quartz substrate with patterned coordinates. Using dark field microscopy, we locate well-spaced individual nanostructures and we determine by SEM that they are single LNO nanocubes. For the subsequent measurements, we record the positions of only single LNO nanocubes that are at least 10 μm apart from all other structures on the substrate. We measure their size with SEM (Figure 1a) and atomic force microscopy (AFM).

Linear Extinction Measurements. We measure the linear scattering cross-section of single LNO nanocubes by using a dark field spectroscopy setup that we adapt for an extended detection range in the NUV. The schematic of the UV-extended setup is shown in Figure S2. We equip the body of an inverted transmission microscope with UV-compatible optical components. We employ aluminum-coated mirrors, and we use fused silica lenses to collimate a xenon arc lamp with high emission efficiency in the UV range. We use a 50× apochromat objective to collect the scattered light with less chromatic aberrations than the standard achromat objectives. We detect the linear scattering spectrum with an imaging spectrometer equipped with a CCD camera containing an extended UV window.

The measured linear scattering cross-section spectra of the LNO nanocubes from Figure 1a are shown in Figure 1b−e. Remarkably, we detect scattering resonances below 400 nm in the NUV. To better understand the scattering cross-section of the single LNO nanocubes and the nature of the scattering peaks, we perform finite element method (FEM) simulations.

DOI: 10.1021/acsphotonics.8b01594
ACS Photonics 2019, 6, 545−552

The simulation model considers an LNO nanocube on a fused quartz substrate. The length, width, and height of the nanocube are set to the values deduced from SEM and AFM micrographs, respectively. The model calculates the scattered field from the LNO nanocube and integrates the Poynting vector over a solid angle corresponding to the numerical aperture of the collection objective (Figure S4e). Furthermore, using a FEM model described elsewhere,[13] the expansion of the scattering cross-section into individual spherical harmonics according to Mie theory[7] allows us to calculate the contributions from individual multipoles. The calculated scattering cross-sections for the LNO nanocubes (cubes 1−4) are shown in Figure 1f−i. The numerical simulations show that a strong scattering efficiency is expected below 400 nm for every LNO nanocube, which is confirmed by the linear measurements. Furthermore, an additional peak above 400 nm followed by a shoulder is observed both in the measurements and in the simulations for the LNO nanocubes with sizes less than 300 nm. The size estimation error of each nanocube causes differences between the measured and simulated spectra. Our FEM simulations show that a size difference as small as 20 nm leads to a shift of the peaks of about 25 nm. Indeed, the measured spectra of cubes 1 and 2 (Figure 1b,c) appear blue-shifted by 20−30 nm. As a consequence, the peak expected below 400 nm for cube 1 (Figure 1f) is not observed. In the case of cube 2, the expected peak below 400 nm (Figure 1g) is observed, but with a reduced intensity. For cubes 3 and 4, we observe a good agreement between measurements and simulations, especially below 450 nm. We compare the UV extended setup with a previously used standard dark field spectroscopy setup[8,13] (Figure S3). We observe that the measurement range of the UV extended setup is increased down to 350 nm, corresponding to a 90 nm extension of the measurement range. The upper limit of the measurement range is determined by the detection sensitivity limit of the CCD camera of the imaging spectrometer, which is around 1050 nm. A further improvement of the dark field spectroscopy setup in the UV range is challenging because of the lack of objectives that have both a high transmission in the UV range and no chromatic aberrations across the UV to visible range.

The results of the spherical multipole expansion are shown in Figure 1j for cube 1 and in Figure S4 for all the other LNO nanocubes presented in this work. For the smaller LNO nanocubes 1 to 3, the linear scattering cross-section continuum between 450 and 650 nm is the result of overlapping contributions from the electric and magnetic dipoles and quadrupoles. The peak appearing between 350 and 450 nm consists of overlapping contributions from the magnetic dipole, electric quadrupole, and electric and magnetic octupoles. A similar behavior is observed in cube 4, but, due to its larger size, the peak and the continuum are shifted further in the visible range. The strong overlap between the multipole contributions is a consequence of the refractive index value of LNO, which, compared to Si, GaAs, or Ge, has smaller values (2.4 at 400 nm).[24] This overlap between the magnetic dipole and octupole, and the electric quadrupole in the case of the LNO nanocubes, also has a significant impact on the SHG efficiency, as demonstrated in the following part. Finally, in comparison to higher refractive index nanostructures, the scattering cross-section also contains a continuum (for instance, from 450 to 600 nm for cube 1, Figure 1b). This makes LNO nanocubes promising structures for broad-spectrum applications such as spectroscopy.

Second-Harmonic Generation Measurements. As we show that the measured LNO nanocubes scatter light efficiently in the NUV range, we investigate if the nonlinear response from the nanocubes is also strong in this range by measuring the SHG signal from the individual LNO nanocubes 1 to 4. For this, we use a home-built SHG transmission microscope setup (Figure S5). Prior to full SHG spectra measurements, we show that the signal emitted from a single LNO nanocube consists only of the SHG response by detecting the emission spectrum of a single nanocube with an imaging spectrometer (Figure S6).

First, we measure the SHG spectrum by sweeping the full laser wavelength range from 700 to 1040 nm in steps of 10 nm and recording the corresponding SHG spanning from 350 to 520 nm. We determine the SHG conversion efficiency γ by dividing the measured SHG power by the squared laser power. The values of γ for all LNO nanocubes 1 to 4 are shown in Figure 2a−d. The data are normalized to the spectral

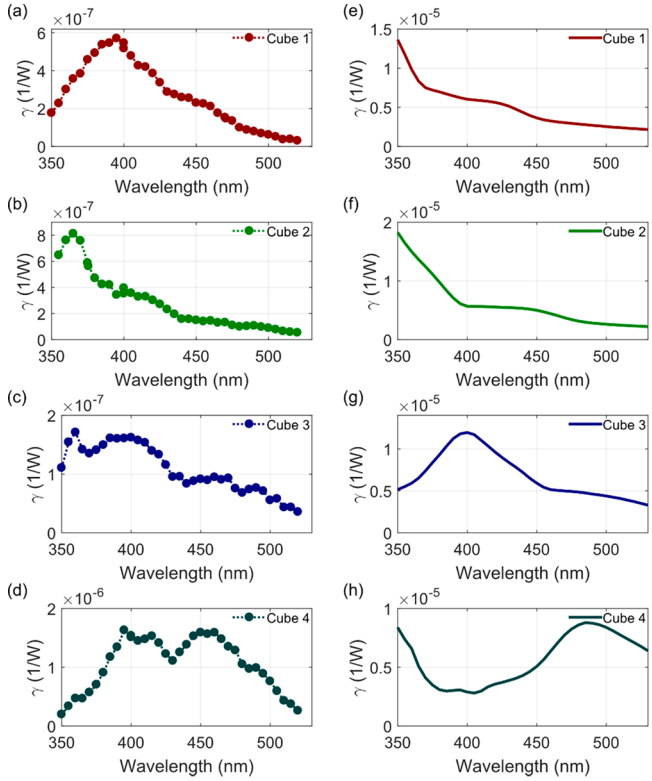

Figure 2. SHG from single LNO nanocubes. (a−d) Measured SHG conversion efficiency γ and (e−h) the simulated SHG conversion efficiency γ of the single LNO nanocubes from Figure 1a. The labels indicate to which nanocube the measurement and simulation correspond.

sensitivity of the experimental setup. The normalization procedure and the calculation of γ are detailed in Supporting Information, S3, where we also estimate the effective second-order susceptibility $\chi^{(2)}_{\mathrm{eff}}$ (Figure S7). All LNO nanocubes demonstrate efficient SHG emission below 400 nm, particularly the cubes smaller than 300 nm. The measured SHG spectra are also compared to numerical simulations (Figure 2e−h) done with an FEM model. To calculate the SHG from a single LNO cube, we determine the second-order polarization from the second-order susceptibility tensor $\chi^{(2)}$ (Supporting Information, S4) and the electric field distribution of the

DOI: 10.1021/acsphotonics.8b01594
ACS Photonics 2019, 6, 545−552

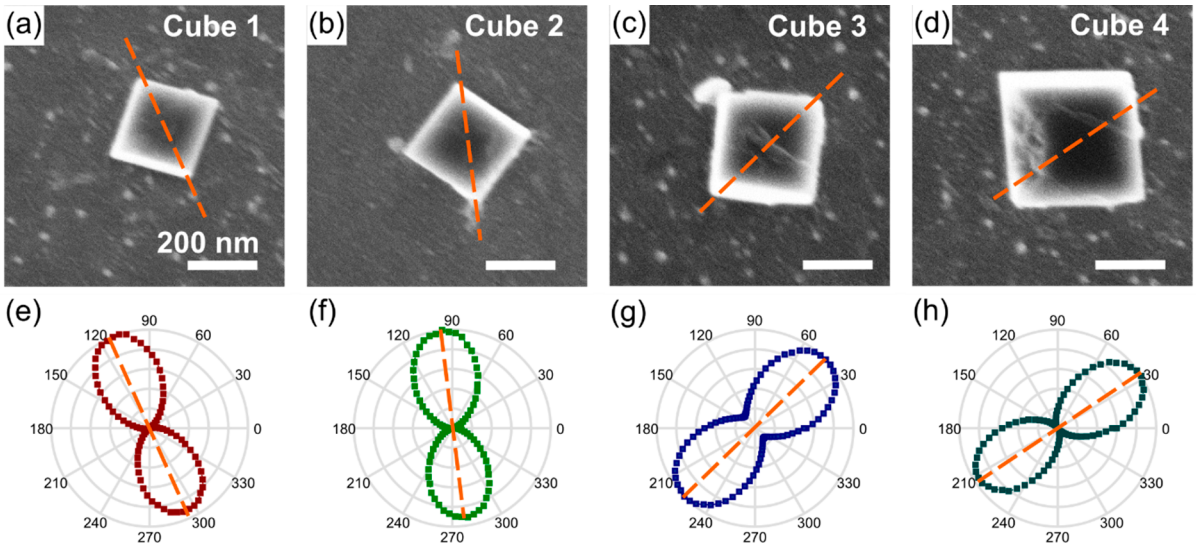

Figure 3. SHG polar plots of single LNO nanocubes. (a–d) SEM images of single LNO nanocubes and (e–h) the corresponding SHG polarization dependence at 400 nm. The dashed orange lines serve as a guide to the eye.

incident light inside the nanocube. The second-order polarization acts as an electromagnetic wave source that radiates into the far field. The SHG power is obtained by integrating the Poynting vector of this source over the solid angle corresponding to the numerical aperture of the collection objective. This method is described in detail in previous works.[13,52] We extended this method by taking the crystal orientation of the LNO nanocube into account (Supporting Information, S4).

The results of the simulated SHG conversion efficiency γ are shown in Figure 2e–h and Figure S4 (thick dotted lines). By comparing the calculated linear scattering cross-section with the calculated SHG conversion efficiency, we observe that the SHG intensity increases significantly around the Mie resonances consisting of the overlap of four multipole contributions (magnetic dipole, electric quadrupole, electric and magnetic octupoles). Additionally, the SHG conversion efficiency has a shoulder at the overlap between the electric and magnetic quadrupoles (for example, at 425 nm for cube 1 in Figure S4a). The major features of the calculated SHG spectra are reproduced by the SHG measurements (Figure 2a–d). For cubes 1, 2, and 3 we observe a peak in the SHG intensity from 350 to 450 nm, depending on the cube size, followed by a shoulder and a subsequent faster decrease. However, compared to the calculated values, the SHG peaks of cubes 1 and 4 are red-shifted by 75 nm and blue-shifted by 35 nm, respectively. Here, the estimation error of the LNO nanocube sizes leads to a shift of the peak position of 20–30 nm (calculated using the FEM model), which cannot fully explain the significant shift in the case of cube 1. Furthermore, we observe an additional peak at 400 nm in the SHG spectrum of cube 4. A likely reason for these discrepancies is the morphology of the LNO nanocubes. For example, cube 4 (Figure 1a) has a defect along one edge (indicated by the orange arrow), which reduces its geometric symmetry. Also, it cannot be excluded that a single nanocube consists of two or more domains that have maximum SHG emission efficiency at different wavelengths. Nevertheless, all measured LNO nanocubes have significant SHG conversion efficiency values between 1.7×10^{-7} and 7.6×10^{-7} 1/W at 360 nm, in the NUV region, for an incident peak irradiance of 1.7 GW/cm^2. The simulation of the SHG conversion efficiency predicts even bigger values around 10^{-5} 1/W for the measured γ. We attribute this difference to multiple causes. First, the LNO nanocube size estimation error causes about 30–50% variations of the measured γ. Second, the excitation in the experiment is done with a focused Gaussian beam, whereas in the simulation we assume a linearly polarized plane wave. Furthermore, the LNO nanocubes have morphological defects such as missing material along edges. Finally, any imperfections in the alignment of the SHG measurement setup causes a reduction of the measured γ.

Additionally, we measure the SHG enhancement of an LNO nanocube compared to a bulk LNO crystal by detecting their SHG at 360 nm. We normalize these signals by the squared SHG emitting volume, which is deduced from the SEM and AFM images for the LNO nanocube. In the case of the LNO crystal, the SHG emitting volume is estimated to a cylinder with a radius equal to the incident laser beam waist and a height equal to the Rayleigh length.[8] We find an SHG enhancement value of 10^7. This enhancement is the result of the electric field confinement in the nanostructure at the SHG wavelength (Figure S8), so that the LNO nanocube acts as a dielectric nanoantenna and increases the SHG radiation to the far field.[8]

The efficient SHG emission in the NUV range is therefore another feature of interest of the LNO cube for NUV photonic applications. Moreover, for LNO nanocubes with sizes below 250 nm, the SHG emission in the NUV range is even more efficient than in the visible range. This is a consequence of the refractive index value of LNO. For materials such as LNO, which have a lower refractive index than Si, Ge, or GaAs, the electromagnetic field is more confined inside the nanostructure for lower wavelengths that correspond to the higher multipole resonances (Figure S8) where the LNO nanocube interacts more efficiently with the incident electromagnetic field. As the SHG enhancement in harmonic nanoparticles is a consequence of the electromagnetic field confinement in the volume at Mie resonances,[8] the SHG signal in the NUV will be higher than in the visible–infrared.

Due to its tensorial nature, the SHG is highly dependent on the crystal orientation of the material. Therefore, we

DOI: 10.1021/acsphotonics.8b01594
ACS Photonics 2019, 6, 545–552

investigate the dependence of the SHG signal on the polarization of the incident laser beam. We rotate the polarization of the incident laser beam using a half-wave plate, and we measure the SHG at 400 nm for each LNO nanocube (Figure 3). Remarkably, for all the tested LNO nanocubes, the maximal SHG is obtained when the incident electromagnetic field is polarized along the diagonal of the top face of the LNO nanocube. In the case of cube 4 (Figure 3d), there is a small angular displacement between the diagonal of the top face of the nanocube and the axis of the SHG polar plot (Figure 3d). This, together with the SHG spectrum of cube 4 (Figure 2d), strongly indicates that this cube has morphological defects that lead to the discrepancies of its optical properties compared to cubes 1 to 3.

The orientation of the SHG polar plots confirms the link between the crystal lattice orientation and the geometrical shape of the LNO nanocubes, which prescribes that the faces of the nanocubes correspond to well-defined families of lattice planes. The polar *c*-axis of the LNO crystal and the major diagonal of the nanocube are parallel. This indicates that the maximum SHG intensity is obtained when the projection of the incident electromagnetic field on the polar *c*-axis is maximized. For this particular orientation of the incident electromagnetic field we exploit the d_{33} component of the reduced $\chi^{(2)}$ tensor of LNO, which has a significantly larger value than the rest of the tensor components (−34 pm/V compared to the next closest one at −4.88 pm/V; see Supporting Information, S4). The SHG polarimetry plots combined with the HRTEM measurements (Figure S1b) indicate that LNO nanocubes placed on a flat surface have three equivalent orientations depending on which of the (012), (−102), and (1−12) faces the nanocube stands. This feature increases the control and predictability of the SHG emission for applications, as the randomness of the crystalline orientation typical of spherical nanostructures is not present.

In summary, we show that LNO nanocubes with sizes from 200 to 300 nm have efficient linear and nonlinear scattering in the NUV range, with nonlinear conversion efficiencies as large as 7.6×10^{-7} 1/W and a 10^7 SHG enhancement compared to bulk LNO at 360 nm. Further, we characterized the linear and SHG spectra of single LNO nanocubes both experimentally and numerically, demonstrating their optical properties using the Mie theory formalism. The numerical analysis completed by the spherical multipole expansion of the linear scattering cross-section shows that multiple Mie resonances contribute to the total scattering cross-section and that these resonances are highly tunable with the size of the nanocubes. The high-order Mie resonances lead to a strong SHG enhancement that can be achieved in the NUV region for nanocubes with sizes around 200 nm. Furthermore, due to the link between the crystal structure and the geometry of these LNO nanocubes, they have predictable crystal orientation. The LNO nanocubes shown in this work are promising multifunctional single emitters for nonlinear photonics at the nanoscale in combination with previously demonstrated LNO nanowires and waveguides[27,53,54] for NUV range applications such as sum-frequency generation, single-photon sources, or nano-optical modulators. Moreover, as an affordable and abundant powder material, they can serve as building blocks of metasurfaces, which can be obtained by capillarity-assisted particle assembly,[52,55] or composite materials for random scattering[56] in a wider wavelength range that is not accessible with typical semiconductor or other dielectric materials.

METHODS

Fabrication of LNO Nanocubes. We fabricate LNO powders by a solvothermal synthesis method. We disperse 3 g of Nb_2O_5 (H.C. Starck, 99.92%) and 0.689 g of LiOH (Aldrich, 98%) in 60 cm^3 of ethylene glycol. The suspension is ultrasonicated for 5 min, poured in a PTFE-lined stainless-steel acid digestion bomb (model PA4748, volume 120 mL, Parr Instrument Company), and hydrothermally treated at 250 °C for 70 h. After cooling, the reaction product is washed several times with water. The final powder suspension is then freeze-dried.

UV-Extended Dark Field Spectroscopy. We built a dark field spectroscopy setup that has an extended detection range in the UV. The schematic of the UV-extended setup is shown in Figure S2. The light from the xenon arc lamp (150 W, Gilden Photonics) is focused onto the sample using a condenser (Zeiss 20× Epiplan-Neofluar dark field objective with an opaque disk to block the center of the light beam). We place an aperture in front of the lamp to create a virtual light source and avoid imaging the lamp electrodes at the sample position. The light scattered by the sample is collected with a 50× objective (Zeiss 50× Epiplan-Apochromat) and detected by a standard camera to check the nanoparticle position and an imaging spectrometer (Princeton Instruments Acton S303 spectrograph) equipped with a CCD camera with an extended UV window (Pixis:256E). The 200 μm core fiber of the imaging spectrometer acts as a pinhole, which allows us to detect only the signal from individual LNO cubes (Figure S2, inset). For each measurement, we adjust the position of single LNO cubes using a CMOS camera. The linear scattering cross-section spectra are obtained by normalizing the signal from a single LNO nanocube to the signal coming directly from the lamp, after subtraction of the background near the LNO nanocube and the dark current counts of the camera.

SHG Measurements. We measure the SHG from individual LNO nanocubes using a home-built SHG microscope. The setup is shown in Figure S5. The laser beam from a pulsed Ti:sapphire laser (Spectra Physics MaiTai DeepSee) is focused onto an LNO nanocube using a lens (f = 25 mm). The SHG and the transmitted laser beam are collected by a 100× objective (Zeiss Neofluar NA = 0.75). The laser beam is removed using a colored glass bandpass filter (Schott BG39), and the SHG signal is measured with a scientific CMOS camera (Andor Zyla 4.2). We control the polarization of the incident laser beam with a half-wave plate mounted on a motorized rotation stage. We test the emission spectrum from a single nanocube excited by the laser beam to confirm that only SHG is emitted. For this, we measure the signal collected by the objective with an imaging spectrometer (Princeton Instruments Acton S303 spectrograph equipped with a CCD camera Pixis:256E).

ASSOCIATED CONTENT

Supporting Information

The Supporting Information is available free of charge on the ACS Publications website at DOI: 10.1021/acsphotonics.8b01594.

Crystal lattice characterization of LNO nanocubes; UV-extended dark field spectroscopy and SHG measurement setups; normalization procedure and calculation of the effective second-order susceptibility; second-order sus-

DOI: 10.1021/acsphotonics.8b01594
ACS Photonics 2019, 6, 545−552

ceptibility tensor of LNO; electric field inside the LNO nanocubes at the Mie resonances (PDF)

AUTHOR INFORMATION

Corresponding Author

*E-mail: ftimpu@phys.ethz.ch.

ORCID

Flavia Timpu: 0000-0002-0951-4070
Claude Renaut: 0000-0003-4143-0480
Maria Timofeeva: 0000-0001-7192-8322
Rachel Grange: 0000-0001-7469-9756

Present Address

⊥Laboratory for Nanometallurgy, ETH Zurich, Vladimir Prelog Weg 1-5/10, 8093 Zürich, Switzerland.

Author Contributions

R.G. and F.T. designed and supervised the experiment. M.T.B. and V.B. fabricated the nanoparticles and performed the XRD and HRTEM measurements. F.T., J.S., and C.R. performed the linear measurements. F.T. performed the nonlinear measurements. F.T. analyzed the data. F.T., L.L., and M.T. carried out the simulations. F.T. wrote the manuscript in collaboration with all the authors. All authors have given approval to the final version of the manuscript.

Notes

The authors declare no competing financial interest.

ACKNOWLEDGMENTS

The authors acknowledge the support of the Scientific Center for Optical and Electron Microscopy (ScopeM) of the Swiss Federal Institute of Technology (ETHZ). This work was supported by the Swiss National Science Foundation grant 150609 and bilateral grant 163916. The project has received funding from the European Research Council under the Grant Agreement No. 714837 Chi2-Nano-Oxide. We thank Adelina Ianculescu, Polytechnic University of Bucharest, for the TEM images of LNO nanocubes.

REFERENCES

(1) Sutherland, R. L. *Handbook of Nonlinear Optics*, 2nd ed.; Marcel Dekker, Inc.: New York, 2003; Vol. 35. https://doi.org/10.1021/cr900335q.Size.

(2) Boyd, R. W. *Nonlinear Optics*; Academic Press, 2003.

(3) Houe, M.; Townsend, P. D. An Introduction To Methods of Periodic Poling for Second-Harmonic Generation. *J. Phys. D: Appl. Phys.* **1995**, *28* (9), 1747−1763.

(4) Baudrier-Raybaut, M.; Haïdar, R.; Kupecek, P.; Lemasson, P.; Rosencher, E. Random Quasi-Phase-Matching in Bulk Polycrystalline Isotropic Nonlinear Materials. *Nature* **2004**, *432* (7015), 374−376.

(5) Suchowski, H.; O'Brien, K.; Jing Wong, Z.; Salandrino, A.; Yin, X.; Zhang, X. Phase Mismatch − Free Nonlinear Propagation in Optical Zero-Index Materials. *Science* **2013**, *342*, 1223−1226.

(6) Zheludev, N. I.; Kivshar, Y. S. From Metamaterials to Metadevices. *Nat. Mater.* **2012**, *11* (11), 917−924.

(7) Bohren, C. F.; Huffman, D. R. *Absorption and Scattering of Light by Small Particles*; John Wiley & Sons, 2008.

(8) Timpu, F.; Sergeyev, A.; Hendricks, N.; Grange, R. Second-Harmonic Enhancement with Mie Resonances in Perovskite Nanoparticles. *ACS Photonics* **2017**, *4*, 76−84.

(9) Liu, S.; Saravi, S.; Keeler, G. A.; Sinclair, M. B.; Yang, Y.; Reno, J.; Pertsch, T.; Brener, I. Resonantly Enhanced Second-Harmonic Generation Using III-V Semiconductor All-Dielectric Metasurfaces. *Nano Lett.* **2016**, *16* (9), 5426−5432.

(10) Gili, V. F.; Carletti, L.; Locatelli, A.; Rocco, D.; Finazzi, M.; Ghirardini, L.; Favero, I.; Gomez, C. Monolithic AlGaAs Second-Harmonic Nanoantennas. *Opt. Express* **2016**, *24* (14), 6488−6492.

(11) Smirnova, D. A.; Khanikaev, A. B.; Smirnov, L. A.; Kivshar, Y. S. Multipolar Third-Harmonic Generation Driven by Optically Induced Magnetic Resonances. *ACS Photonics* **2016**, *3* (8), 1468−1476.

(12) Shcherbakov, M. R.; Neshev, D. N.; Hopkins, B.; Shorokhov, A. S.; Staude, I.; Melik-Gaykazyan, E. V.; Decker, M.; Ezhov, A. A.; Miroshnichenko, A. E.; Brener, I.; et al. Enhanced Third-Harmonic Generation in Silicon Nanoparticles Driven by Magnetic Response. *Nano Lett.* **2014**, *14* (11), 6488−6492.

(13) Timofeeva, M.; Lang, L.; Timpu, F.; Renaut, C.; Bouravleuv, A.; Shtrom, I.; Cirlin, G.; Grange, R. Anapoles in Free-Standing III-V Nanodisks Enhancing Second-Harmonic Generation. *Nano Lett.* **2018**, *18* (6), 3695−3702.

(14) Miroshnichenko, A. E.; Evlyukhin, A. B.; Yu, Y. F.; Bakker, R. M.; Chipouline, A.; Kuznetsov, A. I.; Luk'yanchuk, B.; Chichkov, B. N.; Kivshar, Y. S. Nonradiating Anapole Modes in Dielectric Nanoparticles. *Nat. Commun.* **2015**, *6*, 1−8.

(15) Butet, J.; Brevet, P. F.; Martin, O. J. F. Optical Second Harmonic Generation in Plasmonic Nanostructures: From Fundamental Principles to Advanced Applications. *ACS Nano* **2015**, *9* (11), 10545−10562.

(16) Khurgin, J. B. How to Deal with the Loss in Plasmonics and Metamaterials. *Nat. Nanotechnol.* **2015**, *10* (1), 2−6.

(17) Canfield, B. K.; Husu, H.; Laukkanen, J.; Bai, B.; Kuittinen, M.; Turunen, J.; Kauranen, M. Local Field Asymmetry Drives Second-Harmonic Generation in Noncentrosymmetric Nanodimers. *Nano Lett.* **2007**, *7* (5), 1251−1255.

(18) Butet, J.; Bachelier, G.; Russier-Antoine, I.; Jonin, C.; Benichou, E.; Brevet, P. F. Interference between Selected Dipoles and Octupoles in the Optical Second-Harmonic Generation from Spherical Gold Nanoparticles. *Phys. Rev. Lett.* **2010**, *105* (7), 1−4.

(19) Kuznetsov, A. I.; Miroshnichenko, A. E.; Brongersma, M. L.; Kivshar, Y. S.; Luk'yanchuk, B. Optically Resonant Dielectric Nanostructures. *Science* **2016**, *354* (6314), 846.

(20) Jahani, S.; Jacob, Z. All-Dielectric Metamaterials. *Nat. Nanotechnol.* **2016**, *11* (1), 23−36.

(21) Decker, M.; Staude, I.; Falkner, M.; Dominguez, J.; Neshev, D. N.; Brener, I.; Pertsch, T.; Kivshar, Y. S. High-Efficiency Dielectric Huygens' Surfaces. *Adv. Opt. Mater.* **2015**, *3* (6), 813−820.

(22) Baranov, D. G.; Zuev, D. A.; Lepeshov, S. I.; Kotov, O. V.; Krasnok, A. E.; Evlyukhin, A. B.; Chichkov, B. N. All-Dielectric Nanophotonics: The Quest for Better Materials and Fabrication Techniques. *Optica* **2017**, *4* (7), 814.

(23) Weber, M. J. *Handbook of Optical Materials*; CRC Press, 2002; Vol. 19.

(24) Palik, E. D. Lithium Niobate. In *Handbook of Optical Constants of Solids I*; Academic Press, 1997; pp 695−702. https://doi.org/10.1007/978-3-540-70766-0.

(25) Weis, R. S.; Gaylord, T. K. Lithium Niobate: Summary of Physical Properties and Crystal Structure. *Appl. Phys. A: Solids Surf.* **1985**, *37*, 191−203.

(26) Wang, C.; Zhang, M.; Stern, B.; Lipson, M.; Loncar, M. *Opt. Express* **2018**, *26* (2), 1547−1555.

(27) Reig Escalé, M.; Pohl, D.; Sergeyev, A.; Grange, R. Extreme Electro-Optic Tuning of Bragg Mirrors Integrated in Lithium Niobate Nanowaveguides. *Opt. Lett.* **2018**, *43* (7), 1515−1518.

(28) Kroesen, S.; Horn, W.; Imbrock, J.; Denz, C. Electro−optical Tunable Waveguide Embedded Multiscan Bragg Gratings in Lithium Niobate by Direct Femtosecond Laser Writing. *Opt. Express* **2014**, *22* (19), 23339.

(29) Afanasiev, P. Synthesis of Microcrystalline LiNbO3 in Molten Nitrate. *Mater. Lett.* **1998**, *34* (3−6), 253−256.

(30) Ali, R. F.; Gates, B. D. Synthesis of Lithium Niobate Nanocrystals with Size Focusing through an Ostwald Ripening Process. *Chem. Mater.* **2018**, *30* (6), 2028−2035.

(31) Aufray, M.; Menuel, S.; Fort, Y.; Eschbach, J.; Rouxel, D.; Vincent, B. New Synthesis of Nanosized Niobium Oxides and

DOI: 10.1021/acsphotonics.8b01594
ACS Photonics 2019, 6, 545−552

Lithium Niobate Particles and Their Characterization by XPS Analysis. *J. Nanosci. Nanotechnol.* **2009**, *9* (8), 4780−4785.
(32) Kar, S.; Logad, S.; Choudhary, O. P.; Debnath, C.; Verma, S.; Bartwal, K. S. Preparation of Lithium Niobate Nanoparticles by High Energy Ball Milling and Their Characterization. *Univers. J. Mater. Sci.* **2013**, *1* (2), 18−24.
(33) Knabe, B.; Buse, K.; Assenmacher, W.; Mader, W. Spontaneous Polarization in Ultrasmall Lithium Niobate Nanocrystals Revealed by Second Harmonic Generation. *Phys. Rev. B: Condens. Matter Mater. Phys.* **2012**, *86* (19), 1−9.
(34) Liu, M.; Xue, D. A Solvothermal Route to Crystalline Lithium Niobate. *Mater. Lett.* **2005**, *59* (23), 2908−2910.
(35) Mohanty, D.; Chaubey, G. S.; Yourdkhani, A.; Adireddy, S.; Caruntu, G.; Wiley, J. B. Synthesis and Piezoelectric Response of Cubic and Spherical LiNbO3 Nanocrystals. *RSC Adv.* **2012**, *2* (5), 1913.
(36) Wang, Y.; Zhou, X. Y.; Chen, Z.; Cai, B.; Ye, Z. Z.; Gao, C. Y.; Huang, J. Y. Synthesis of Cubic LiNbO3 Nanoparticles and Their Application in Vitro Bioimaging. *Appl. Phys. A: Mater. Sci. Process.* **2014**, *117* (4), 2121−2126.
(37) Staedler, D.; Magouroux, T.; Hadji, R.; Joulaud, C.; Extermann, J.; Schwung, S.; Passemard, S.; Kasparian, C.; Clarke, G.; Gerrmann, M.; et al. Harmonic Nanocrystals for Biolabeling: A Survey of Optical Properties and Biocompatibility. *ACS Nano* **2012**, *6* (3), 2542−2549.
(38) Rogov, A.; Mugnier, Y.; Bonacina, L. Harmonic Nanoparticles: Noncentrosymmetric Metal Oxides for Nonlinear Optics. *J. Opt.* **2015**, *17* (3), No. 033001.
(39) Timofeeva, M.; Bouravleuv, A.; Cirlin, G.; Shtrom, I.; Soshnikov, I.; Reig Escalé, M.; Sergeyev, A.; Grange, R. Polar Second-Harmonic Imaging to Resolve Pure and Mixed Crystal Phases along GaAs Nanowires. *Nano Lett.* **2016**, *16* (10), 6290−6297.
(40) Brasselet, S. Polarization-Resolved Nonlinear Microscopy: Application to Structural Molecular and Biological Imaging. *Adv. Opt. Photonics* **2011**, *3*, 205−271.
(41) Brasselet, S.; Zyss, J. Nano-Crystals for Quadratic Nonlinear Imaging: Characterization and Applications. In *Nanocrystals*; InTech, 2010.
(42) Liu, T. M.; Conde, J.; Lipiński, T.; Bednarkiewicz, A.; Huang, C. C. Revisiting the Classification of NIR-Absorbing/Emitting Nanomaterials for in Vivo Bioapplications. *NPG Asia Mater.* **2016**, *8* (8), 1−25.
(43) Bonacina, L. Nonlinear Nanomedecine: Harmonic Nanoparticles toward Targeted Diagnosis and Therapy. *Mol. Pharmaceutics* **2013**, *10* (3), 783−792.
(44) Hsieh, C.-L.; Pu, Y.; Grange, R.; Laporte, G.; Psaltis, D. Imaging through Turbid Layers by Scanning the Phase Conjugated Second Harmonic Radiation from a Nanoparticle. *Opt. Express* **2010**, *18* (20), 20723−20731.
(45) Grange, R.; Lanvin, T.; Hsieh, C.-L.; Pu, Y.; Psaltis, D. Imaging with Second-Harmonic Radiation Probes in Living Tissue. *Biomed. Opt. Express* **2011**, *2* (9), 2532−2539.
(46) Staedler, D.; Magouroux, T.; Passemard, S.; Schwung, S.; Dubled, M.; Schneiter, G. S.; Rytz, D.; Gerber-Lemaire, S.; Bonacina, L.; Wolf, J. P. Deep UV Generation and Direct DNA Photo-Interaction by Harmonic Nanoparticles in Labelled Samples. *Nanoscale* **2014**, *6* (5), 2929−2936.
(47) Mahou, P.; Malkinson, G.; Chaudan, É.; Gacoin, T.; Beaurepaire, E.; Supatto, W. Metrology of Multiphoton Microscopes Using Second Harmonic Generation Nanoprobes. *Small* **2017**, *13* (42), 1−11.
(48) Akselrod, G. M.; Huang, J.; Hoang, T. B.; Bowen, P. T.; Su, L.; Smith, D. R.; Mikkelsen, M. H. Large-Area Metasurface Perfect Absorbers from Visible to Near-Infrared. *Adv. Mater.* **2015**, *27* (48), 8028−8034.
(49) Ginn, J. C.; Brener, I.; Peters, D. W.; Wendt, J. R.; Stevens, J. O.; Hines, P. F.; Basilio, L. I.; Warne, L. K.; Ihlefeld, J. F.; Clem, P. G.; et al. Realizing Optical Magnetism from Dielectric Metamaterials. *Phys. Rev. Lett.* **2012**, *108* (9), 1−5.
(50) Marino, G.; Solntsev, A. S.; Xu, L.; Gili, V.; Carletti, L.; Poddubny, A. N.; Smirnova, D.; Haitao, C.; Zhang, G.; Zayats, A. V.; et al. Sum-Frequency Generation and Photon-Pair Creation in AlGaAs Nano-Disks. In *2017 Conference on Lasers and Electro-Optics Europe & European Quantum Electronics Conference (CLEO/Europe-EQEC)*; IEEE: Munich, 2017; pp 1−1.
(51) Reig Escalé, M.; Sergeyev, A.; Geiss, R.; Grange, R. Nonlinear Mode Switching in Lithium Niobate Nanowaveguides to Control Light Directionality. *Opt. Express* **2017**, *25* (4), 3013.
(52) Timpu, F.; Hendricks, N. R.; Petrov, M.; Ni, S.; Renaut, C.; Wolf, H.; Isa, L.; Kivshar, Y.; Grange, R. Enhanced Second-Harmonic Generation from Sequential Capillarity-Assisted Particle Assembly of Hybrid Nanodimers. *Nano Lett.* **2017**, *17* (9), 5381−5388.
(53) Sergeyev, A.; Geiss, R.; Solntsev, A. S.; Sukhorukov, A. A.; Schrempel, F.; Pertsch, T.; Grange, R. Enhancing Waveguided Second-Harmonic in Lithium Niobate Nanowires. *ACS Photonics* **2015**, *2* (6), 687−691.
(54) Sergeyev, A.; Reig Escalé, M.; Grange, R. Generation and Tunable Enhancement of a Sum-Frequency Signal in Lithium Niobate Nanowires. *J. Phys. D: Appl. Phys.* **2017**, *50*, No. 044002.
(55) Ni, S.; Wolf, H.; Isa, L. Programmable Assembly of Hybrid Nanoclusters. *Langmuir* **2018**, *34* (7), 2481−2488.
(56) Beaudoux, F.; Ferrier, A.; Guillot-Noël, O.; Chanelière, T.; Le Gouët, J.-L.; Goldner, P. Emission of Photon Echoes in a Strongly Scattering Medium. *Opt. Express* **2011**, *19* (16), 15236.

DOI: 10.1021/acsphotonics.8b01594
ACS Photonics 2019, 6, 545−552